MIT Open Access Articles

A Water-Soluble NaCMC/NaPAA Binder for Exceptional Improvement of Sodium-Ion Batteries with an SnO2-Ordered Mesoporous Carbon Anode

Author Manuscript

Title: Water-soluble NaCMC/NaPAA binder for exceptional improvements of sodium-ion battery with SnO2–ordered mesoporous carbon anode

Authors: Jagabandhu Patra; Purna Chandra Rath; Chi Li; Hsien-Ming Kao; Fu-Ming Wang; Ju Li; Jeng-Kuei Chang, Ph.D.

Water-soluble NaCMC/NaPAA binder for exceptional improvements of sodium-ion battery with SnO₂–ordered mesoporous carbon anode

Water-soluble NaCMC/NaPAA binder for exceptional improvements of sodium-ion battery with SnO$_2$–ordered mesoporous carbon anode

Jagabandhu Patra [a,b,f], Purna Chandra Rath [a,b], Chi Li [a], Hsien-Ming Kao [c], Fu-Ming Wang [d], Ju Li [e], Jeng-Kuei Chang [a,b,e,f*]*

[a] Institute of Materials Science and Engineering, National Central University, Taoyuan, Taiwan
[b] Department of Materials Science and Engineering, National Chiao Tung University, Hsinchu, Taiwan
[c] Department of Chemistry, National Central University, Taoyuan, Taiwan
[d] Graduate Institute of Applied Science and Technology, National Taiwan University of Science and Technology, Taipei, Taiwan
[e] Department of Nuclear Science and Engineering and Department of Materials Science and Engineering, Massachusetts Institute of Technology, Cambridge, MA 02139, USA
[f] Hierarchical Green-Energy Materials (Hi-GEM) Research Centre, National Cheng Kung University, Tainan, Taiwan

[*]Corresponding authors:

Address: 77 Massachusetts Avenue, Massachusetts Institute of Technology, Cambridge, MA 02139, USA
E-mail: liju@mit.edu (Ju Li)

Address: 1001 Ta-Hsuch Road, National Chiao Tung University, Hsinchu 30010, Taiwan
E-mail: jkchang@nctu.edu.tw (Jeng-Kuei Chang)

Keywords: sodium battery, electrode mechanical integrity, binder wetting and spreading

SnO$_2$@CMK-8 composite, a highly promising anode for Na-ion batteries (NIBs), is incorporated with polyvinylidene difluoride (PVDF), sodium carboxymethylcellulose (NaCMC), sodium polyacrylate (NaPAA), and NaCMC/NaPAA mixed binders to optimize the electrode sodiation/desodiation properties. Synergistic effects between NaCMC and NaPAA lead to the formation of an effective protective film on the electrode. This coating layer not only increases

the charge–discharge Coulombic efficiency, suppressing the accumulation of solid-electrolyte interphases, but also keeps the SnO_2 nanoparticles in the CMK-8 matrix, preventing oxide agglomeration and falling off upon cycling. The adhesion strength and stability towards the electrolyte of the binders are evaluated. In addition, the charge-transfer resistance and apparent Na^+ diffusion of the SnO_2@CMK-8 electrodes with various binders are examined and post-mortem analyses are conducted. With NaCMC/NaPAA binder, exceptional electrode capacities of 850 and 425 mAh g^{-1} are obtained at charge–discharge rates of 20 and 2000 mA g^{-1}, respectively. After 300 cycles, 90% capacity retention is achieved. The thermal reactivity of the sodiated electrodes is studied using differential scanning calorimetry. The binder effects on NIB safety, in terms of thermal runaway, are discussed.

1. Introduction

Rechargeable Na-ion batteries (NIBs) is an appealing alternative or complementary technology to lithium-ion batteries (LIBs) for large-scale energy storage. [1,2] The main incentive for using NIBs is the abundance, global distribution, and low cost of sodium precursors.[3] However, NIBs are still in the early stages of development. For example, although there has been decent progress on cathode materials, including layered oxides, polyanionic compounds, Prussian blue analogues, and organic compounds,[4–8] finding a good anode is relatively challenging since the commonly used LIB graphite anode has poor Na^+ storage capability.[9,10] In addition to electrode materials, there are many components in NIBs, such as binders, conductive agents, electrolytes, additives, and separators.[11–15] These seemingly minor parts greatly affect the performance of NIBs.[16]

2

In general, the main function of polymer binders is to glue the active materials and conductive agents to the current collector, to maintain mechanical integrity, simultaneous electronic and ionic percolation, and to reduce thickness expansion. The importance of binders is usually overlooked, since they account for only ~5 wt% of the electrode material and essentially contribute little to capacity.[11,17,18] Polyvinylidene difluoride (PVDF) is a widely used binder in LIBs due to its acceptable bonding capability and electrochemical stability.[19] PVDF is usually dissolved in volatile, flammable, and toxic *N*-methyl-pyrrolidone (NMP) solvent for electrode slurry preparation, which requires special care of the processing conditions, and thus has a high production cost.[18,20] Moreover, both PVDF and NMP are expensive and difficult to recycle. For NIB applications, it has been reported that PVDF tends to defluorinate during sodiation, leading to loss of electrode integrity.[21] In this context, new water-soluble binders have recently attracted a lot of attention for LIBs and NIBs due to their low cost, nontoxicity, short drying time, easy processing, and great bonding ability.[22–26] It is noted that cost-effectiveness and large-scale applications are emphasized for NIBs. Using appropriate and inexpensive binders (which account for only ~5 wt% of electrodes) to improve battery performance is thus more desirable than developing sophisticated active materials for the same purpose. The radius of Na^+ (1.02 Å) is larger than that of Li^+ (0.76 Å), and thus the electrode volume variation upon charging/discharging for NIBs is higher than that for LIBs.[27] This implies that binders can play a more significant role in determining performance for NIBs. All these factors justify the importance of further study about water-soluble binders for NIBs.

SnO_2 has attracted much attention as an NIB anode because it is chemically stable, readily available, and nontoxic, and has a high theoretical capacity.[28–31] Recently, the present authors proposed a unique three-dimensional (3D) architectured SnO_2@CMK-8 electrode with a high tap

3

density.[32] CMK stands for "Carbon Mesostructured by KAIST", to mark the contribution from KAIST, Korea, to template-assisted fabrications of mesoporous carbons.[33] The CMK-8 is a kind of 3-D mesoporous carbon with an *Ia3d* symmetry, which can be prepared by using ordered porous silica KIT-6 as the hard template for nanocasting.[34] With optimized electronic and ionic conduction in the electrode, SnO$_2$ nanoparticles (NPs) underwent a conversion reaction (SnO$_2$ + 4Na$^+$ + 4e$^-$ ↔ Sn + Na$_2$O) and then an alloying reaction (Sn +3.75Na$^+$ + 3.75e$^-$ ↔ ¼Na$_{15}$Sn$_4$), resulting in a reversible capacity of as high as 800 mAh g^{-1}.[32] This electrode is quite promising, even though PVDF binder was used. However, there are some issues (e.g., relatively low (~55%) first-cycle Coulombic efficiency (CE), limited rate capability, and non-ideal cycling stability) that must be overcome before practical applications become feasible. The effects of binder selection on the electrochemical performance of a SnO$_2$-based NIB anode are still unclear; various binders have been arbitrarily chosen in the literature (PVDF is the most common).[35–37] The only study on binders for SnO$_2$ anodes showed that polyacrylic acid (PAA)–soluble starch (SS) binder was superior to the conventional PDVF binder in terms of electrode durability.[38] However, the SnO$_2$ capacity was relatively low (i.e., 370 mAh g^{-1}@100 mA g^{-1}), so the volume expansion/shrinkage during cycling was relatively gentle (less harsh on binders). A more systematic and detailed investigation is called for.

Binder selection can be electrode-material-specific. Komaba et al. found that a hard carbon anode with sodium carboxymethyl cellulose (NaCMC) binder has better reversibility and cyclability than those of an electrode with PVDF binder.[21] With NaCMC binder, the hard carbon derived from cherry petals showed a high initial capacity of 310 mAh g^{-1} and great cycling stability.[39] NaCMC binder was also found to improve the CE, rate capability, and stability of a Na$_2$Ti$_6$O$_{13}$ anode.[40] It was recently reported that a Na$_3$V$_2$(PO$_4$)$_2$F$_3$ cathode with NaCMC binder

4

has excellent high-rate performance and cycle life (i.e., 75 mAh g^{-1}@70 C and 79% capacity retention after 3500 cycles).[24] In addition, NaCMC binder was found to be also suitable for phosphorus/carbon nanotube (CNT), PbTiO$_3$, and Na$_{0.44}$MnO$_2$ electrodes.[41,42,25] However, opposite results have also been reported; for example, a sodium Prussian blue/PVDF electrode showed superior charge–discharge performance to that with NaCMC binder.[43] Contradictory results have also been reported for sodium polyacrylate (NaPAA) binder, which can outperform PAA binder due to its more favorable polymer conformation and the fact that Na$^+$ can improve the solid-electrolyte interphase (SEI) properties.[23,44] N-doped CNT[45] and FeS$_2$[26] anodes with NaPAA binder exhibited excellent capacity, CE, and cycling stability, whereas an Sn-Co anode with the same binder showed poor durability.[46] An appropriate binder must thus be selected for a given electrode material to optimize electrochemical performance. The development of a good binder for high-capacity SnO$_2$ anodes of NIBs is the goal of the present work.

The thermochemical stability of sodiated anodes is a crucial property that affects thermal runaway in practical NIBs. Two key factors are of major concern: (i) the exothermic onset temperature, which governs the initial step that triggers a fire/explosion, and (ii) the total heat released, which is indicative of the magnitude of reaction enthalpy.[47,48] Both factors are associated with the thermal stability of the SEI layer.[47,48] Since the binder can affect SEI chemistry,[49] it is expected that electrode thermal reactivity will vary with binder type. This topic, however, has received little attention to date. The present study first investigates this issue for NIBs using differential scanning calorimetry (DSC). PVDF, NaCMC, NaPAA, and mixed NaCMC/NaPAA binders are systematically compared in terms of crystallinity, bonding strength, stability, and the resulting electrode morphology, surface chemistry, impedance, and sodiation/desodiation properties.

5

2. Results and discussion

Figure 1(a) shows the wide-angle XRD pattern of the SnO_2@CMK-8 sample. All peaks are attributed to various crystallographic planes of standard tetragonal SnO_2 (JCPDS 41-1445). The crystallinity of CMK-8 is too low to exhibit distinct diffraction signals. The broad peaks indicate that SnO_2 had a small crystal size. The microstructure of SnO_2@CMK-8 examined with TEM is shown in **Figure 1(b)**. The SnO_2 NPs (dark spots), with a uniform size of approximately $2(\pm1)$ nm, were highly dispersed and well confined within the 3D porous CMK-8 matrix (bright framework). The SnO_2-to-CMK-8 weight ratio was found to be approximately 85:15.[32] The small-angle XRD data for pristine CMK-8 and SnO_2@CMK-8 samples are shown in **Figure S2**. The intensities of the 1.1° and 1.3° peaks, which corresponded to (211) and (220) superlattice diffractions, respectively, of the CMK-8 highly ordered mesoporous structure with an *Ia3d* symmetry,[50] significantly decreased after SnO_2 incorporation. This confirms that most of the mesopores of CMK-8 were filled with SnO_2 NPs.

The thermal stability of the binders was evaluated with TGA; the obtained data are shown in **Figure S3**. Considering the hydrophilicity of NaCMC and NaPAA, the gradual weight loss before ~150 °C for the two binders can be attributed to the removal of absorbed water. NaCMC showed the lowest decomposition temperature (about 300 °C), producing Na_2O and Na_2CO_3.[51] PVDF decomposed at ~420 °C with a huge weight drop of > 60%. NaPAA had the highest thermal stability (i.e., the smallest weight loss, 25%, at the highest temperature, 460 °C). It is noted that for any binder, the decomposition temperature is much higher than that used for slurry drying (i.e., ~100 °C), and thus binder thermal stability is not an issue during the electrode fabrication process.

6

The bonding ability of the binders was evaluated using peel tests. Scotch tape was adhered to the electrode, and then manually peeled off to test the adhesion. As shown in **Figure S4**, for the PVDF sample, the active material layer was mostly removed from the substrate. With NaCMC binder, the adhesion between Cu foil and the coating material layer was improved. However, the connection between the SnO_2@CMK-8 NPs was still not strong, as a clearly detached film was found on the tape side. NaPAA binder enhanced the inter-particle adhesion even more, since the amount of SnO_2@CMK-8 on the tape was reduced. The highest adhesion strength was found for NaCMC/NaPAA mixed binder. The carbonyl and carboxyl groups on the binders can form hydrogen bonds between the polymer chains and interact with SnO_2 and the current collector to maintain mechanical stability.[17,52] In addition to being an adhesive, NaCMC is also a dispersant,[11,53] which can modify the conformation of the mixed binder and increase the number of bonding sites with the active material and Cu foil, which reduces the flaw size[54] and leads to excellent adhesion of the electrode.

Figure 2(a) shows the initial five CV curves of the SnO_2@CMK-8 electrode with NaCMC/NaPAA binder. In the first negative scan, there were small humps around 1.5–2.0 V, which were associated with the surface group reduction at the electrode. The irreversible peak at ~0.8 V can be attributed to FEC decomposition and SEI formation.[13,55] A conversion reaction of SnO_2 with Na^+ then occurred, which formed Sn and Na_2O. When the potential was scanned towards even lower voltage (< 0.3 V), another cathodic peak arose, indicating the occurrence of Sn–Na alloying reactions (forming $NaSn_5$, NaSn, Na_9Sn_4, $Na_{15}Sn_4$, etc.).[56,57] Below 0.1 V, Na^+ insertion into the carbon phase can also take place.[58] In the following positive scan, the reverse reactions (i.e., desertion, dealloying, and re-conversion) occurred, contributing to the anodic peaks. The CV redox behavior became stable in the subsequent scans. The voltammetric

7

characteristics of the SnO₂@CMK-8 electrodes with other binders are similar, as shown in **Figure S5**.

The charge–discharge curves of various SnO₂@CMK-8 electrodes (for the initial five cycles) are shown in **Figure 2(b)** and **Figure S6**. The Coulombic inefficiency (CI ≡ 1–CE) was ascribed to the partial trapping of Na in SnO₂ and the formation of an SEI layer (i.e., electrolyte decomposition).[28,30] **Figure 2(c)** indicates that the first-cycle CE values for the PVDF, NaCMC, NaPAA, and NaCMC/NaPAA electrodes are 53%, 60%, 62%, and 70%, respectively. The initial efficiency of 70% is among the best reported in the literature (the mechanism is discussed later), with efficiencies of 30–45% being common for various SnO₂-based NIB anodes.[30,38,55,59,60] At the fifth cycle, a CE of 99.3% was obtained for the NaCMC/NaPAA electrode at a low charge–discharge rate of 20 mA g^{-1}. The data suggest that an appropriate binder can accommodate the volume change and modify the surface chemistry of SnO₂@CMK-8, improving the reversibility of the electrode.

XPS was used to examine the surface chemical composition of the electrodes. The C 1s spectra of the as-prepared electrodes are shown in **Figure 3(a)**. The peak at ~284.6 eV corresponds to the binding energy of C–C and C–H bonds.[61,62] The PVDF electrode exhibited strong signals at 285.5 and 290.6 eV, which can be attributed to –CH₂– and –CF₂– bonds, respectively.[61] For the aqueous binder electrodes, the 286.7 eV peak is associated with C–O bonding (for NaCMC), and the 288.5 eV peak is ascribed to the –COONa group (for both NaCMC and NaPAA).[21,63] **Figure 3(b)** presents the Sn 3d spectra of the electrodes, which show similar binding energies for all binders. The 3d$^{5/2}$ and Sn 3d$^{3/2}$ peaks located at 487.5 and 496.1 eV, respectively, confirm that the valence of Sn was +4.[32,64] Interestingly, the normalized peak intensity for electrodes decreased in the sequence PVDF > NaCMC > NaPAA >

8

NaCMC/NaPAA. These results suggest that the NaCMC/NaPAA electrode was best covered by the binder layer, decreasing the signals from the underlying SnO_2. The co-existence of NaCMC and NaPAA led to a synergistic improvement in homogeneous wetting of the binder on active particle surface, consistent with the adhesion testing results (**Figure S4**) before cycling.

Figure 3(c) compares the surface-exposed Sn content levels of various electrodes before and after five charge–discharge cycles. It was found that the surface Sn concentration of the PVDF electrode was considerably reduced after cycling, whereas that of the NaCMC/NaPAA electrode remained almost unchanged. Continuous electrolyte decomposition (suggested by the low CE; **Figure 2(c)**), and thus the growth of the SEI layer, is responsible for the clear decrease in the Sn ratio of the PVDF electrode. **Figure 3(d)** shows the F spectra of the cycled electrodes. The peak at ~687.6 eV for the PVDF electrode is associated with its $-CF_2-$ bond.[65,66] All the electrodes showed a new signal at ~684.1 eV after cycling, corresponding to NaF within SEI, which originated from electrolyte decomposition.[66,67] The low NaF intensity for the NaCMC/NaPAA electrode further supports the suppressed SEI growth.

Figure 4 illustrates the electrode microstructure development. Due to the crystalline nature (see **Figure S7**) and bundle formation of PVDF chains,[61,62] PVDF binder cannot uniformly cover the electrode surface. The electrolyte easily permeated through PVDF and came into direct contact with the electrode material, leading to a large electrolyte decomposition reaction and high CI, especially in the first cycle. Moreover, this SEI layer did not seem to be robust enough to withstand the SnO_2 volume change upon charging/discharging (according to **Figure 2(c)).** The repeated breakdown and re-formation of the SEI layer led to its thickening like a snow cover. In contrast, NaCMC and NaPAA binders are fully amorphous (**Figure S7**) and can form a relatively continuous surface coating layer because of better wetting and spreading properties on particle

9

surface, which acted like an artificial SEI layer (since these binders are reasonable ionic conductors but poor electronic conductors), improving electrode passivation. In addition, this layer was mechanically stable, minimizing the growth of the SEI layer.

The charge−discharge curves (after five conditioning cycles) of the SnO_2@CMK-8 electrodes measured at various rates are shown in **Figure 5(a)** and **Figure S8**. At 20 mA g^{-1}, the measured discharge (desodiation) capacities were 795, 800, 810, and 850 mAh g^{-1} for the electrodes with PVDF, NaCMC, NaPAA, and NaCMC/NaPAA binders, respectively. NaCMC/NaPAA mixed binder is most suitable for the SnO_2@CMK-8 electrode. With the unique 3D mesoporous architecture and appropriate selection of functional binder, the obtained electrode capacity of 850 mAh g^{-1} is superior to most reported values.[30,35–38,55,59,60,64] The great bonding ability of the binder can increase the active material utilization. The thin SEI layer facilitated Na^+ transport across the electrode/electrolyte interface.[65] Moreover, the carbonyl and carboxyl groups of the binders may partially participate in the sodiation/desodiation reaction.[68] As a result, the NaCMC/NaPAA electrode had great charge–discharge capacity.

The electrode's volumetric specific capacity is also a concern for practical battery applications. The compressed densities of the PVDF, NaCMC, NaPAA, and NaCMC/NaPAA layers were 0.40, 0.47, 0.47, and 0.48 g cm^{-3}, respectively (including binder and carbon black). The water-soluble binders can more closely pack the active material particles and reduce the inter-particle space in the electrodes (as illustrated in **Figure 4**). The volumetric capacities of these electrodes were calculated to be 254, 301, 311, and 326 mAh cm^{-3} at 20 mA g^{-1}, respectively. Nanostructured materials usually exhibit low volumetric performance. However, the experimental data confirm that our anode with an appropriate binder has a much higher

10

volumetric capacity than that (130 mAh cm^{-3}) of a hard carbon electrode, which is the most popular NIB anode studied in the literature.[69]

The binder effects on the rate capability of the SnO$_2$@CMK-8 electrodes are shown in **Figure 5(b)**. At a high rate of 2000 mA g^{-1}, the electrodes with PVDF, NaCMC, NaPAA, and NaCMC/NaPAA binders had reversible capacities of 325, 345, 365, and 425 mAh g^{-1}, corresponding to 41%, 43%, 45, and 50% retention, respectively, compared to the values measured at 20 mA g^{-1}. The reasons for the performance variation were determined using EIS. As revealed in the Nyquist plots of **Figure 5(c)**, the spectra consisted of a semicircle at high frequency and a sloping line at low frequency, which can be characterized by the equivalent circuit shown in the figure inset, where R_e, R_{ct}, *CPE*, and *W* are the electrolyte resistance, interfacial charge transfer resistance, interfacial constant phase element, and Warburg impedance associated with Na$^+$ diffusion in the electrode, respectively.[30] The R_{ct} values, which are related to the EIS semicircle diameter, were calculated to be 580, 400, 370, and 240 Ω for the PVDF, NaCMC, NaPAA, and NaCMC/NaPAA electrodes, respectively. The PVDF electrode having the largest R_{ct} is attributed to its having the thickest SEI layer (**Figure 3(c)**). The apparent Na$^+$ diffusion coefficients (D_{Na^+}) for the electrodes can be calculated from the oblique linear Warburg parts[64]; the calculated values for these electrodes are 1.7×10^{-16}, 3.8×10^{-15}, 6.1×10^{-15}, and 8.3×10^{-15} cm^2 s^{-1}, respectively. The tightly packed SnO$_2$@CMK-8 NPs can form a favorable Na$^+$ diffusion pathway, which resulted in an enhanced transport rate. The D_{Na^+} values of the PVDF and NaCMC/NaPAA electrodes were also estimated using CV (see **Figure S9** for details). The linear relationship between the redox current and the square root of the CV sweep rate indicates that the sodiation/desodiation reactions are diffusion-controlled. The obtained D_{Na^+} values are

11

7.2×10^{-16} and 1.2×10^{-14} cm^2 s^{-1}, respectively, which are consistent with the EIS data, again confirming the importance of binder selection in achieving the desired electrochemical properties.

The cycling stability of the various SnO$_2$@CMK-8 electrodes was evaluated at 100 mA g^{-1}; the results are shown in **Figure 5(d)**. The capacity retention ratios after 300 cycles are 78%, 83%, 85%, and 90% for the PVDF, NaCMC, NaPAA, and NaCMC/NaPAA electrodes, respectively, with the CE values saturating at 98.6%, 99.1%, 99.2%, and 99.7%, respectively. **Figure 5(e)** reveals the variation of R_{ct} with the number of cycles for the electrodes. The more pronounced R_{ct} increase upon cycling for the PVDF electrode indicates the inferior surface passivation of this electrode. The accumulation of the SEI layer, which not only increased the electrode resistance but also decreased the number of electroactive sites, led to the capacity fading. In contrast, the adhesive and dispersant nature of NaCMC,[11] when mixed with NaPAA, improved wetting and spreading of the binder on the active particle surface. This artificial layer formed was robust and can suppress the SEI evolution, improving the electrode durability. The cycling stability of the electrodes was further examined at a high charge–discharge rate of 2000 mA g^{-1} (**Figure S10**). After 150 cycles, the capacity retention ratios were 56%, 64%, 66%, and 73% for the PVDF, NaCMC, NaPAA, and NaCMC/NaPAA electrodes, respectively. The decreased durability at a high sodiation–desodiation rate suggests that the electrode volume expansion/shrinkage, rather than other parasitic reactions, is mainly responsible for the capacity decay. A good binder, even though it accounts for only a small portion of the electrode, plays a significant role in cycling stability, especially under high-rate operation. Besides the binder selection, the electrode cycling stability can also be improved by development of new electrolyte formulations, electrode architectures, and other pretreatment processes.[16,70,71]

12

Figure S11 compares the surface appearances of the electrodes after 300 charge–discharge cycles. For the PVDF electrode, some of the Cu substrate was exposed (due to the detachment of the active material layer), whereas the NaCMC/NaPAA electrode retained the best mechanical integrity. The corresponding electrode morphologies examined using SEM are shown in **Figure 6**. The PVDF electrode had huge cracks and was covered by a thick SEI layer. The PVDF binder could not withstand the substantial electrode volume change during cycling (**Figures 6(a)**), leading to decohesion and pulverization (see the FIB cross-section image in **Figure 6(e)**). As shown in **Figures 6(b)** and **(c)**, thinner SEI layers and smaller cracks were found for the NaCMC and NaPAA electrodes. The highest structural stability was found for the electrode with NaCMC/NaPAA mixed binder (**Figure 6(d)**). The types of groups on the polymer chains of NaCMC are different from those of NaPAA (**Figure S1**) and thus may provide extra bonding sites. Moreover, NaCMC can act as a dispersant to enhance the uniformity of NaPAA in the electrode slurry.[11,53] As reveled in the cross-section micrograph of **Figure 6(f)**, the active material layer was tightly adhered to the current collector. This confirms that NaCMC/NaPAA mixed binder can buffer the electrode mechanical stresses during cycling and maintain structural integrity, suppressing the growth of the SEI layer.

The stability of the polymer binders was also examined by soaking in the electrolyte; the results are shown in **Figure S12**. The PVDF powder was easily peptized by the electrolyte. This implies that the structural firmness and the conductive pathways of the PVDF electrode can be degraded by electrolyte penetration, especially with high-expansion electrode materials. In contrast, the other water-soluble binders were quite stable in the organic electrolyte and settled down well under the vessels. This property is important for sustaining a robust electrode

13

framework. The stable NaCMC and NaPAA binders can also serve as barrier layers to reduce undesirable parasitic reactions between the SnO$_2$@CMK-8 electrode and the electrolyte.

The SnO$_2$@CMK-8 powder was scraped from the PVDF and NaCMC/NaPAA electrodes after 300 charge–discharge cycles and then subjected to TEM analyses. As shown in **Figure 7**, for the PVDF sample, the SnO$_2$ NPs had escaped from the CMK-8 matrix, leading to agglomeration and separation of the oxide. In contrast, with the NaCMC/NaPAA binder, the microstructure of SnO$_2$@CMK-8 was well preserved. These results suggest that the binder can effectively wrap the SnO$_2$@CMK-8 spheres and keep the SnO$_2$ NPs encapsulated inside the CMK-8 matrix after cycling (as shown in **Figure 4**). The conducting network and electroactive sites for SnO$_2$ can thus be retained, leading to excellent cycling stability of the electrode.

Figure 8 shows the thermal reactivity of the sodiated electrodes with various binders examined with DSC. In general, the following reactions can be distinguished in the DSC profiles with increasing temperature: the original SEI film breakdown, the chemical reaction between the electrolyte and the SEI-free sodiated anode (leading to the formation of a new SEI layer), and the thermal decomposition of this re-formed SEI layer.[47,48] It was found that the original SEI layer of the PVDF electrode decomposed at the lowest temperature (as shown in **Table 2**) with the least heat released. These data indicate that the SEI chemistry is indeed altered by the electrode binder. The reasons for the more exothermic SEI decomposition reactions of the aqueous binder electrodes are unknown; this topic requires further investigation. Interestingly, the reaction enthalpies of the SEI-free anodes and electrolyte (the second DSC peaks) were significantly reduced with the use of the aqueous binders, especially NaCMC/NaPAA. It is believed that the binder layer which effectively wets the electrode surface can decrease direct contact with the electrolyte, suppressing reactivity. The total heat generated, summarized in **Table 2**, for the

14

PVDF, NaCMC, NaPAA, and NaCMC/NaPAA samples is 300, 247, 232, and 195 J g^{-1}, respectively, up to 225 °C. The binder effects on the electrode safety characteristics were demonstrated for NIB applications for the first time in this study.

3. Conclusion

Binder selection was found to be crucial for optimizing the electrochemical performance of the SnO_2@CMK-8 anode for NIBs. NaCMC/NaPAA binder, which is stable in the electrolyte, can effectively wet, spread on the surfaces and tightly glue the SnO_2@CMK-8 particles, increasing the adhesion strength and compressed density of the active material layer. This mixed binder (with synergistic effects) not only withstood the electrode volume variation and maintained structural integrity upon cycling, but also formed a protective layer on the electrode to separate the liquid electrolyte with the active particles and suppress the growth of the SEI layer. Reduced R_{ct} and increased D_{Na}^+ were also found for this electrode, which showed excellent capacity (850 mAh g^{-1} or 326 mAh cm^{-1}), rate capability (425 mAh g^{-1}@2000 mAh g^{-1}), and cycling stability (90% capacity retention after 300 cycles). The use of NaCMC/NaPAA binder also increased the exothermic onset temperature and reduced the total heat generated at the anode, improving the NIB safety. This cost-effective binder has great practical potential for NIB applications.

4. Experimental procedures

4.1. Synthesis of SnO_2@CMK-8 and cell assembly.

SnO_2@CMK-8 was synthesized using procedures described in our previous study.[32] PVDF (Sigma-Aldrich), NaCMC (Sigma-Aldrich), and NaPAA (Kishida Chemicals) binders were used

as received. The molecular structures of the binders are shown in **Figure S1**. The electrode slurry was made up of 80 wt% SnO_2@CMK-8, 10 wt% carbon black, and 10 wt% binder dispersed in either *N*-methyl-2-pyrrolidone (for PVDF) or distilled water (for NaCMC, NaPAA, and NaCMC/NaPAA (1:1 by weight)). The slurry was coated onto Cu foil with a doctor blade and dried at 100 °C for 3 h under vacuum. The final thickness of the active material layers was approximately 65 μm. The active material loading was typically 1–1.2 mg cm^{-2}. This electrode was roll-pressed and then punched to match the required dimensions of a CR2032 coin cell. While preparing the NaCMC/NaPAA electrodes, we did not find any considerable impact of binder mixing sequence on the electrochemical properties. Thick Na foil and a glassy fiber membrane were used as the counter electrode and separator, respectively. The electrolyte was 1 M $NaClO_4$ in propylene carbonate (PC)/ethylene carbonate (EC) mixed solvent (1:1 by volume) with 5 wt% fluoroethylene carbonate (FEC) additive. The assembly of the coin cells was performed in an argon-filled glove box (Innovation Technology Co. Ltd.), where both the moisture and oxygen content levels were maintained at below 0.5 ppm.

4.2. Material and electrochemical characterizations.

The crystallinity of SnO_2@CMK-8 was characterized with X-ray diffraction (XRD; Bruker D8 ADVANCE) using Cu K$_\alpha$ radiation as the incident X-ray source. The small-angle XRD patterns were recorded with a Shimadzu LabX XRD-6000 diffractometer with Cu K$_\alpha$ radiation. The morphology and microstructure of the samples were examined using scanning electron microscopy (SEM; FEI Inspect F50), a focused ion beam (FIB; FEI V ersa 3D), and high-resolution transmission electron microscopy (TEM; JEOL 2100F). X-ray photoelectron spectroscopy (XPS; VG Sigma Probe) was used to analyze surface chemical compositions of the

16

electrodes. The Al K$_\alpha$ radiation (1486.6 eV) was used as the excitation source. All of the acquired spectra were referenced to the C 1s peak of hydrocarbon at a binding energy of 284.6 eV. XPSPEAK 4.1 software was adopted for the data fitting. Thermogravimetric analyses (TGA; PerkinElmer TGA7) were conducted with a heating rate of 5 °C min^{-1} to characterize the thermal stability of the binders. Electrochemical impedance spectroscopy (EIS) was performed in a frequency range of 100 kHz–10 mHz with an AC amplitude of 10 mV. A Biologic VSP-300 potentiostat was used for cyclic voltammetry (CV) measurements. The charge–discharge properties (such as capacity, rate performance, and cycling stability) of various electrodes were evaluated using a battery tester (Arbin, BT–2043) at 25 °C. For each condition, at least five coin cells were tested. The performance deviation was typically within 5%. The reported data are the median values. The thermal reactivity of the sodiated SnO$_2$@CMK-8 samples with various binders was evaluated using DSC (Netzsch DSC3500) in a temperature range of 50–225 °C. The samples were pre-sodiated to 0.01 V vs. Na/Na$^+$, recovered from the coin cells, placed into Al capsules in the glove box without washing and drying, and then transferred to the DSC chamber, which was filled with N$_2$ gas and heated at a rate of 10 °C min^{-1}.

Supporting Information

Supporting Information is available from the Wiley Online Library or from the author.

Acknowledgements

17

References

1. J. W. Choi, D. Aurbach, *Nat. Rev. Mater*. **2016, 1**, 16013.

2. H. Kim, H. Kim, Z. Ding, M.H. Lee, K. Lim, G. Yoon, K. Kang, *Adv. Energy Mater.* **2016**, *6*, 1600943.

3. C. Vaalma, D. Buchholz, M. Weil, S. Passerini, *Nat. Rev. Mater.* **2018**, *3*, 18013.

4. N. Wongittharom, C. H. Wang, Y. C. Wang, C. H. Yang, J. K. Chang, *ACS Appl. Mater. Interfaces* **2014**, *6*, 17564–17570.

5. C. H. Wang, Y. W. Yeh, N. Wongittharom, Y. C. Wang, C. J. Tseng, S. W. Lee, W. S. Chang, J. K. Chang, *J. Power Sources* **2015***, 274*, 1016–1023.

6. H. Y. Li, C. H. Yang, C. M. Tseng, S. W. Lee, C. C. Yang, T. Y. Wu, J. K. Chang**, *J. Power Sources* **2015***, 285*, 418–424.

7. Y. You, A. Manthiram**, *Adv. Energy Mater.* **2017**, *8*, 1701785.

8. P. K. Nayak, L. Yang, W. Brehm, P. Adelhelm, *Angew. Chem. Int. Ed.* **2017**, *57*, 102–120.

9. P. Ge, M. Fouletier, *Solid State Ion.* **1988**, *28-30*, 1172–1175.

10. B. Jache, P. Adelhelm, *Angew. Chem. Int. Ed.* **2014**, *53*, 10169–10173.

11. W. Zhang, M. Dahbi, S. Komaba, *Curr. Opin. Chem. Eng.* **2016***, 13*, 36–44.

12. C. Bommier, X. Ji, Electrolytes, *Small* **2018**, *14*, 1703576.

13. S. Komaba, T. Ishikawa, N. Yabuchi, W. Murata, A. Ito, Y. Ohsawa, *ACS Appl. Mater. Interfaces* **2011**, *3*, 4165–4168.

14. P. Arora, Z. Zhang, *Chem. Rev.* **2004**, *104*, 4419–4462.

15. Q. Zhang, Z. Yu, P. Du, C. Su, *Recent Patents on Nanotechnology* **2010**, *4*, 100–110.

16. J. Y. Hwang, S. T. Myung, Y. K. Sun, *Chem. Soc. Rev.* **2017**, *46*, 3529–3614.

17. S. L. Chou, Y. Pan, J. Z. Wang, H. K. Liu, S. X. Dou, *Phys. Chem. Chem. Phys*. **2014**, *16*, 20347–20359.

18. J. T. Li, Z. Y. Wu, Y. Q. Lu, Y. Zhou, Q. S. Huang, L. Huang, S. G. Sun, *Adv. Energy Mater.* **2017**, *7*, 1701185.

19. N. Yabuuchi, K. Kubota, M. Dahbi, S. Komaba, *Chem. Rev.* **2014**, *114*, 11636–11682.

20. X. Wang, C. Yao, F. Wang, Z. Li, *Small* **2017***, 13*, 1702240.

21. M. Dahbi, T. Nankano, N. Yabuchi, T. Ishikawa, K. Kubota, M. Fukunishi, S. Shibahara, J. Y. Son, Y. T. Cui, H. Oji, S. Komaba, *Electrochem. Commun.* **2014**, *44*, 66–69.

22. Y. Shi, X. Zhou, G. Yu, *Acc. Chem. Res.* **2017**, *50*, 2642–2652.

23. S. Komaba, K. Okushi, T. Ozeki, H. Yui, Y. Katayama, T. Miura, T. Saito, H. Groult, *Electrochem. Solid State Lett.* **2009***, 12*, A107–A110.

24. J. Zhao, X. Yang, Y. Yao, Y. Gao, Y. Sui, B. Zou, H. Ehrenberg, G. Chen, F. Du, *Adv. Sci.* **2018,** 5, 1700768.

25. V. D. Asta, D. Buchholz, L. G. Chagas, X. Dou, C. Ferrara, E. Quartarone, C. Tealdi, S. Passerini, *ACS Appl. Mater. Interfaces* **2017**, *9,* 34891–34899.

26. K. Chen, W. Zhang, L. Xie, W. Chen, X. Xiang, M. Wan, Y. Huang, *ACS Appl. Mater. Interfaces* **2017**, *9*, 1536–1541.

27. S. Y. Hong, Y. Kim, Y. Park, A. Choi, N. S. Choi, K. T. Lee, *Energy Environ. Sci*. **2013**, *6*, 2067–2081.

28. Z. Li, J. Ding, D. Mitlin, *Acc. Chem. Res*. **2015**, *48*, 1657–1665.

29. B. Huang, Z. Pan, X. Su, L. An, *J. Power Sources* **2018**, *395*, 41–59.

30. J. Patra, H. C. Chen, C. H. Yang, C. T. Hsieh, C. Y. Su, J. K. Chang, *Nano Energy* **2016**, *28*, 124–134.

31. X. Li, Z. Zhu, G. P. Nayaka, J. Duan, D. Wang, P. Dong, L. Huang, J. Zhao, S. Sun, X. Yu, Y. Zhang, *J Alloys Compd.* **2018**, *752*, 68–75.

32. J. Patra, P. C. Rath, C. H. Yang, D. Saikia, H. M. Kao, J. K. Chang, *Nanoscale* **2017**, *9*, 8674–8683.

33. R. Ryoo, S. H. Joo, *Stud. Surf. Sci. Catal.* **2004**, *148*, 241–260.

34. P. C. Rath, J. Patra, D. Saikia, M. Mishra, J. K. Chang, H. M. Kao, *J. Mater. Chem. A* **2016**, *4*, 14222–14233.

35. Y. Y. Wang, B. H. Hou, Y. N. Wang, H. Y. Lu, J. Z. Guo, Q. L. Ning, J. P. Zhang, C. L. Lu, X. L. Wu, *J. Mater. Chem. A* **2018**, *6*, 6578–6586.

36. M. Dirican, Y. Lu, Y. Ge, O. Yildiz, X. Zhang, *ACS Appl. Mater. Interfaces* **2015**, *7*, 18387–18396.

37. H. Z. Li, L. Y. Yang, J. Liu, S. T. Li, L. B. Fang, Y. K. Lu, H. R. Yang, S. L. Liu, M. Lei, *J. Power Sources* **2016**, *324*, 780–787.

38. Y. Wei, Z. Wang, H. Ye, J. Mou, D. Lei, Y. Liu, W. Lv, B. Li, F. Kang, Y. B. He, *ChemistrySelect* **2017**, *2*, 11365–11369.

39. Z. Zhu, F. Liang, Z. Zhou, X. Zeng, D. Wang, P. Dong, J. Zhao, S. Sun, Y. Zhang, X. Li, *J. Mater. Chem. A* **2018**, *6*, 1513–1522.

40. Y. Zhang, H. Hou, X. Yang, J. Chen, M. Jing, Z. Wu, X. Jia, X. Ji, *J. Power Sources* **2016**, *305*, 200–208.

41. J. Song, Z. Yu, M. L. Gordin, X. Li, H. Peng, D. Wang, *ACS Nano* **2015**, *9*, 11933–11941.

42. Y. Zhang, M. Ji, Z. Liu, Y. He, Y. Hu, Q. Yang, B. Lia, J. Wang, *RSC Adv.* **2017**, *7*, 25678–25684.

43. M. J. P. Munoz, E. C. Martinez, J. L. G. Camer, T. Rojo, *Electrochim. Acta* **2016**, *200*, 123–130.

44. Z. J. Han, K. Yamagiwa, N. Yabuuchi, J. Y. Son, Y. T. Cui, H. Oji, A. Kogure, T. Harada, S. Ishikawa, Y. Aoki, S. Komaba, *Phys.Chem.Chem.Phys.* **2015**, *17*, 3783–3795.

45. Q. Fan, W. Zhang, J. Duan, K. Hong, L. Xue, Y. Huang, *Electrochim. Acta* **2015**, *174*, 970–977.

46. Y. Yui, M. Hayashi, K. Hayashi, J. Nakamura, *Solid State Ion.* **2016**, *288*, 219–223.

47. A. Ponrouch, E. Marchante, M. Courty, J. M. Tarascona, M. R. Palacın, *Energy Environ. Sci.* **2012**, *5*, 8572–8583.

48. G.G. Eshetu, S. Grugeon, H. Kim, S. Jeong, L. Wu, G. Gachot, S. Laruelle, M. Arman, S. Passerini, *ChemSusChem* **2016**, *9*, 462–471.

49. Y. S. Park, E. S. Oh, S. M. Lee, *J. Power Sources* **2014**, *248*, 1191–1196.

50. F. Kleitz, S. H. Choi, R. Ryoo, *Chem. Commun.* **2003**, *17*, 2136–2137.

51. N. Cuesta, A. Romes, I. Camean, C. Antuna, A. B. Garcia, *Electrochim. Acta* **2015**, *155*, 140–147.

52. N. P. W. Pieczonka, V. Borgel, B. Ziv, N. Leifer, V. Dargel, D. Aurbach, J. H. Kim, Z. Liu, X. Huang, S. A. Krachkovskiy, G. R. Goward, I. Halalay, B. R. Powell, A. Manthiram, *Adv. Energy Mater.* **2015**, *5*, 1501008.

53. L. Chen, X. Xie, J. Xie, K. Wang, J. Yang, *J. Appl Electrochem.* **2006,** *36*, 1099–1104.

54. H. Gao, B. Ji, I. L. Jager, E. Arzt, P. Fratzl, *P. Proc. Natl. Acad. Sci. U.S.A* **2003**, *100*, 5597–5600.

55. H. C. Chen, J. Patra, S. W. Lee, C. J. Tseng, T. Y. Wu, M. H. Lin, J. K. Chang, *J. Mater. Chem. A* **2017**, *5*, 13776–13784.

21

56. J. W. Wang, X. H. Liu, S. X. Mao, J. Y. Huang, *Nano Lett.* **2012**, *12*, 5897–5902.

57. V. L. Chevrier, G. Ceder, *J. Electrochem. Soc.* **2011**, *158*, A1011–A1014.

58. J. Ding, H. Wang, Z. Li, A. Kohandehghan, K. Cui, Z. Xu, B. Zahiri, X. Tan, E. M. Lotfabad, B. C. Olsen, D. Mitlin, *ACS Nano* **2013**, *7*, 11004–11015.

59. Y. X. Wang, Y. G. Lim, M. S. Park, S. L. Chou, J. H. Kim, H. K. Liu, S. X. Dou, Y. J. Kim, *J. Mater. Chem. A* **2014**, *2*, 529–534.

60. J. Ding, Z. Li, H. Wang, K. Cui, A. Kohandehghan, X. Tan, D. Karpuzovc, D. Mitlin, *J. Mater. Chem. A* **2015**, *3*, 7100–7111.

61. N. Yabuchi, K. Shimomura, Y. Shimbe, T. Ozeki, J. Y. Son, H. Oji, Y. Katayama, T. Miura, S. Komaba, *Adv. Energy Mater.* **2011**, *1*, 759–765.

62. S. Komaba, N. Yabuchi, T. Ozeki, Z. J. Han, K. Shimomura, H. Yui, Y. Katayama, T. Miura, *J. Phys. Chem. C* **2012**, *116*, 1380–1389.

63. S. Komaba, K. Shimomura, N. Yabuchi, T. Ozeki, H. Yui, K. Konno, *J. Phys. Chem. C* **2011**, *115*, 13487–13495.

64. L. Fan, X. Li, B. Yan, J. Feng, D. Xiong, D. Li, L. Gu, Y. Wen, S. Lawes, X. Sun, *Adv. Energy Mater.* **2016**, *6*, 1502057.

65. J. Patra, H. T. Huang, W. Xue, C. Wang, A. S. Helal, J. Li, J. K. Chang, *Energy Storage Mater.* **2019**, *7*, 146–154.

66. K Takad, Y. Yamada, E. Watanabe, J. Wang, K. Sodeyama, Y. Tateyama, K. Hirata, T. Kawasa, A. Yamada, *ACS Appl. Mater. Interfaces* **2017**, *9*, 33802–33809.

67. H. Kim, J. S. Park, S. H. Sahgong, S. Park, J. K. Kim, Y. Kim, *J. Mater. Chem. A* **2014**, *2*, 19584–19588.

68. Y. E. Eli, V. R. Koch, *J. Electrochem. Soc.* **1997***, 144*, 2968–2973.

69. X. F. Luo, A. S. Helal, C. T. Hsieh, J. Li, J. K. Chang, *Nano Energy* **2018**, *49*, 515–522.

70. J. Cui, S. Yao, J. K. Kim, *Energy Storage Mater.* **2017**, *7*, 64–114.

71. C. Chen, Y. Wen, X. Hu, X. Ji, M. Yan, L. Mai, P. Hu, B. Shan, Y. Huang, *Nat. Commun.* **2015**, *6*, 6929.

23

Table 1. Charge–discharge properties and film densities of SnO_2@CMK-8 electrodes with various binders.

	PVDF	NaCMC	NaPAA	NaCMC/NaPAA
First-cycle CE	53%	60%	62%	70%
Maximum capacity (C_{20}; at 20 mA g^{-1})	795	800	810	850
High rate capacity (C_{2000}; at 2000 mA g^{-1})	325	345	365	425
Rate capability C_{2000}/C_{20}	41%	43%	45%	50%
Cycling retention (after 300 cycles)	78%	83%	85%	90%
Film density (mg/cm^{-3})	0.40	0.47	0.47	0.48

Author Manuscript

24

Table 2. DSC data of sodiated SnO_2@CMK-8 anodes with various binders evaluated in a temperature range of 50–225 °C.

Binders	Exothermic onset temperature (°C)	Total heat released (J g^{-1})
PVDF	75	300
NaCMC	101	247
NaPAA	101	232
NaCMC/NaPAA	100	195
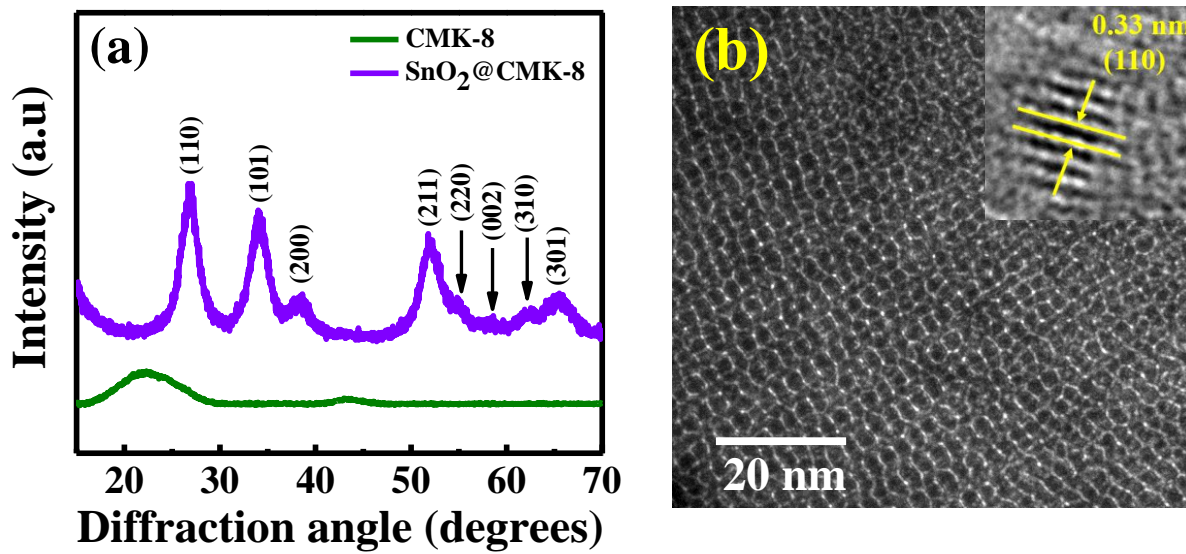
Figure 1. (a) Wide-angle XRD pattern and (b) TEM images of SnO$_2$@CMK-8 composite.

26
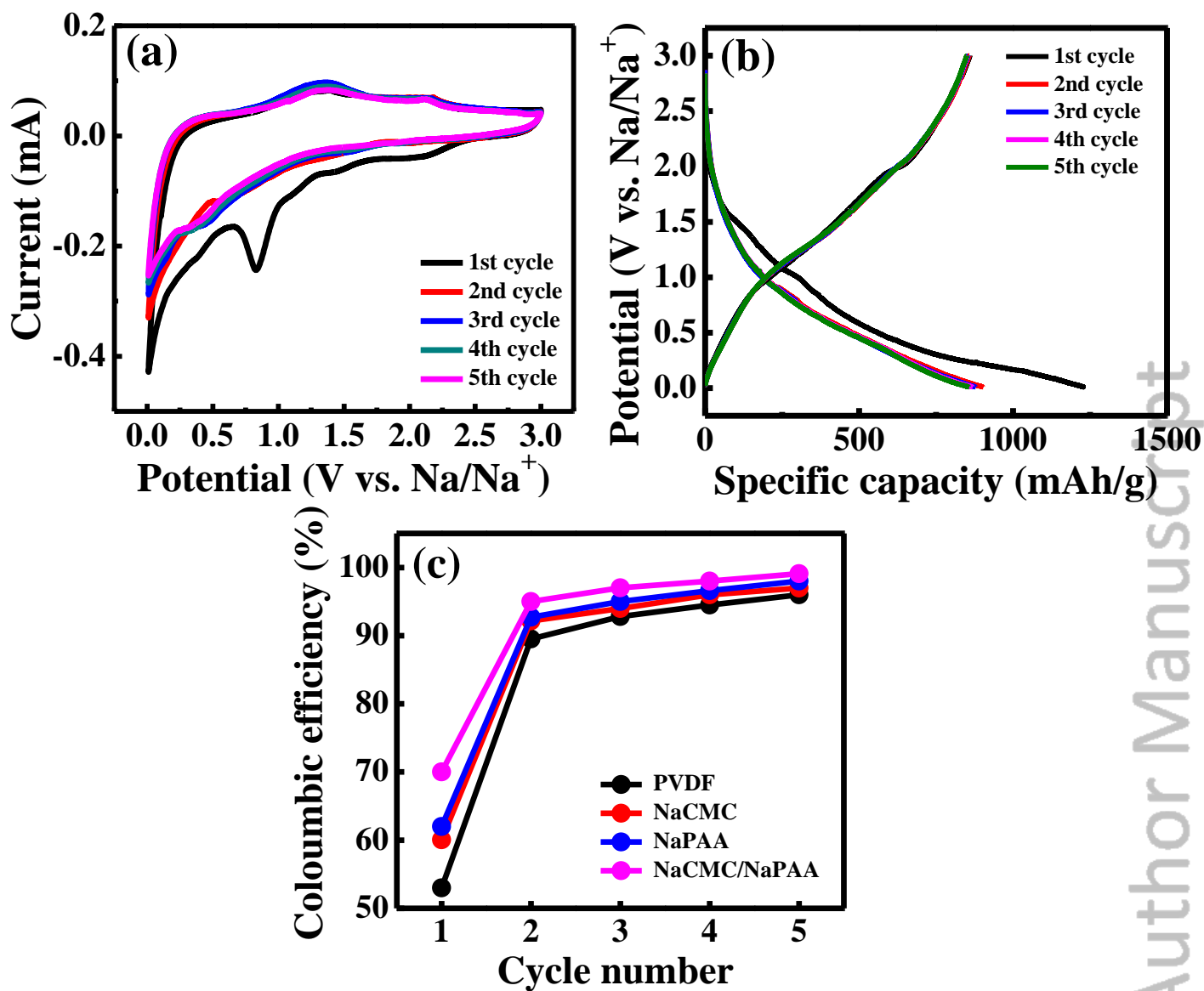
Figure 2. (a) CV curves of NaCMC/NaPAA electrode measured at a scan rate of 0.1 mV s^{-1}. (b) Initial five charge–discharge curves of NaCMC/NaPAA electrode measured at 20 mA g^{-1}. (c) The CE values versus cycle number for the electrodes with various binders.

27
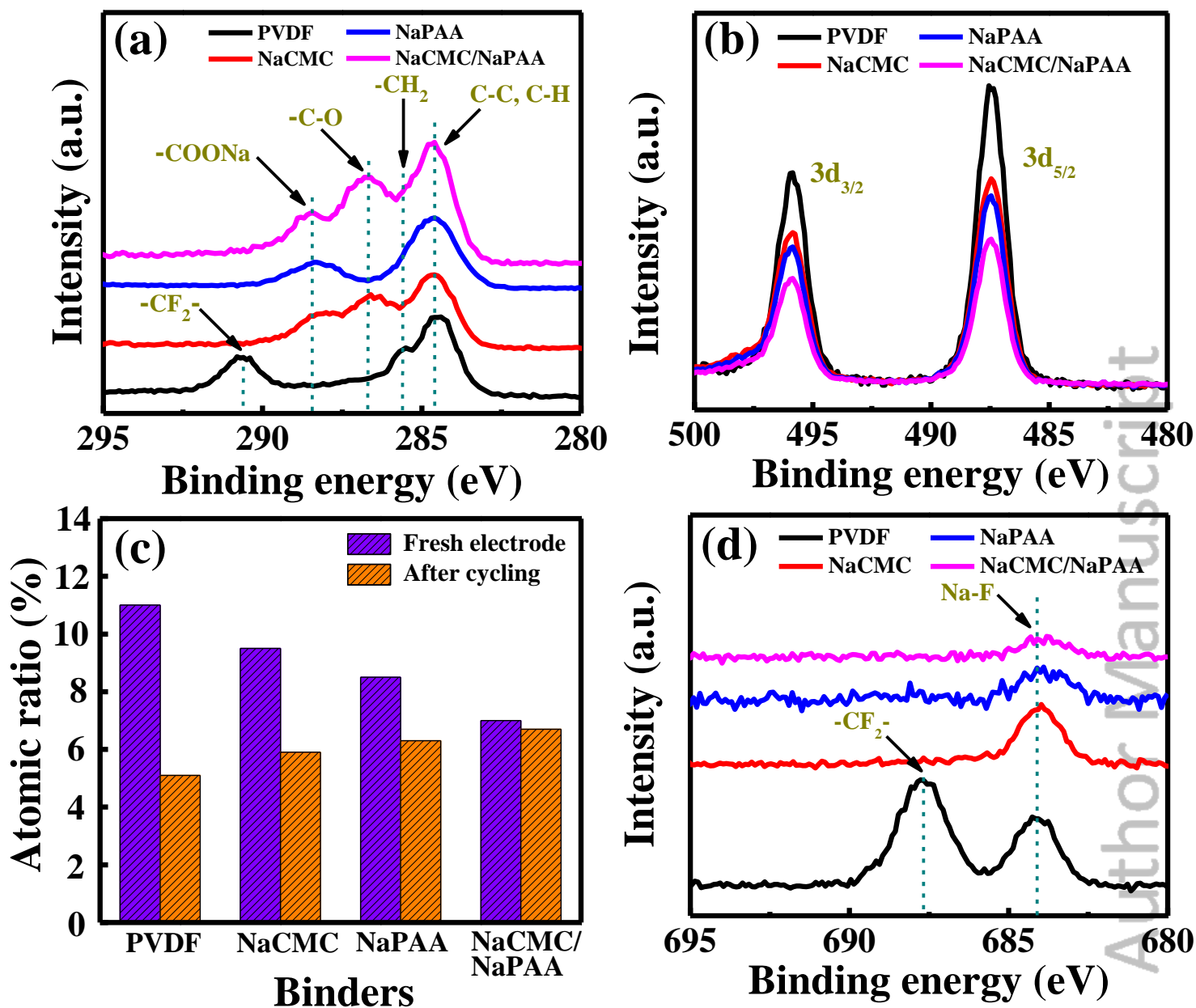
Figure 3. XPS (a) C 1s and (b) Sn 3d spectra of freshly prepared electrodes with various binders. (c) Comparison of Sn concentrations of various electrodes before and after five charge–discharge cycles. (d) XPS F 1s spectra of various electrodes after five charge–discharge cycles.
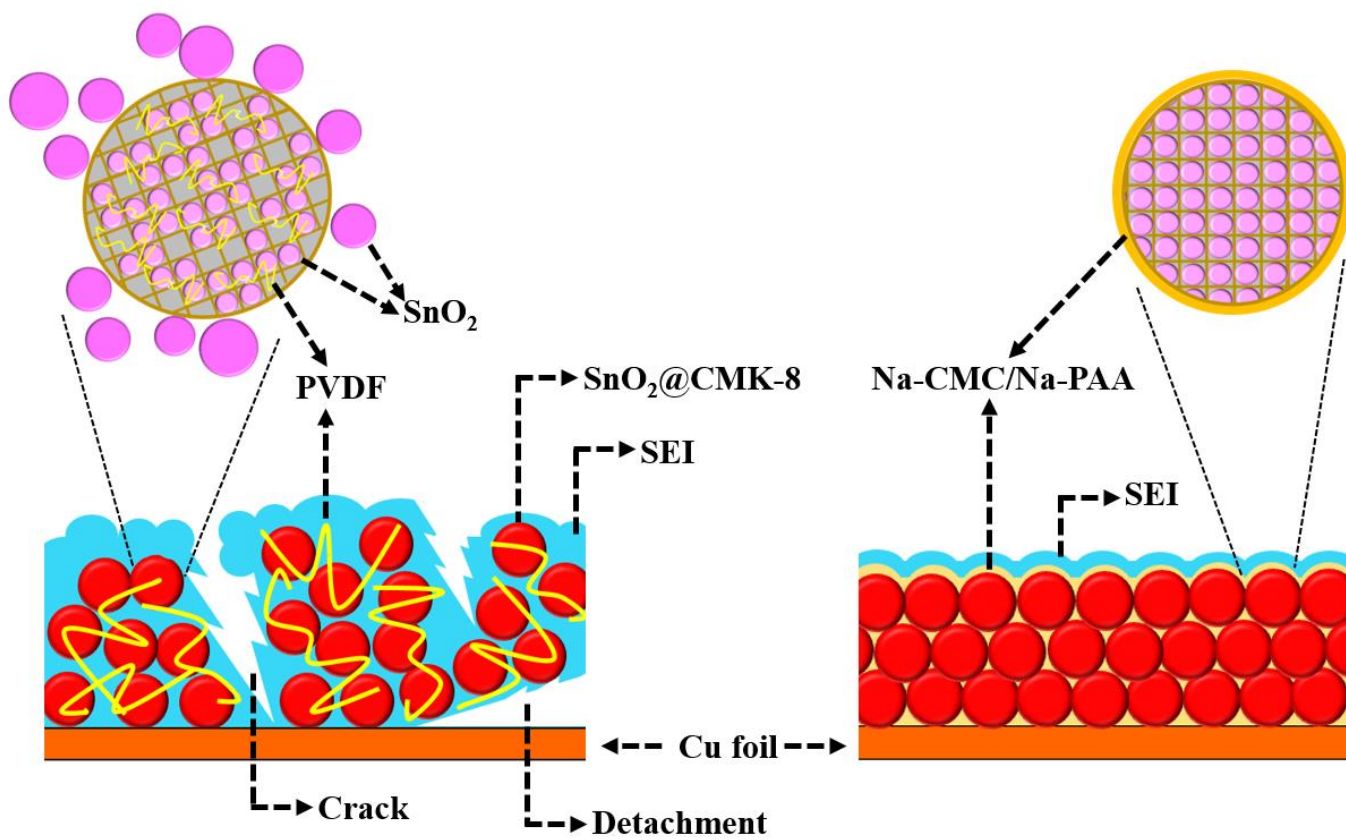
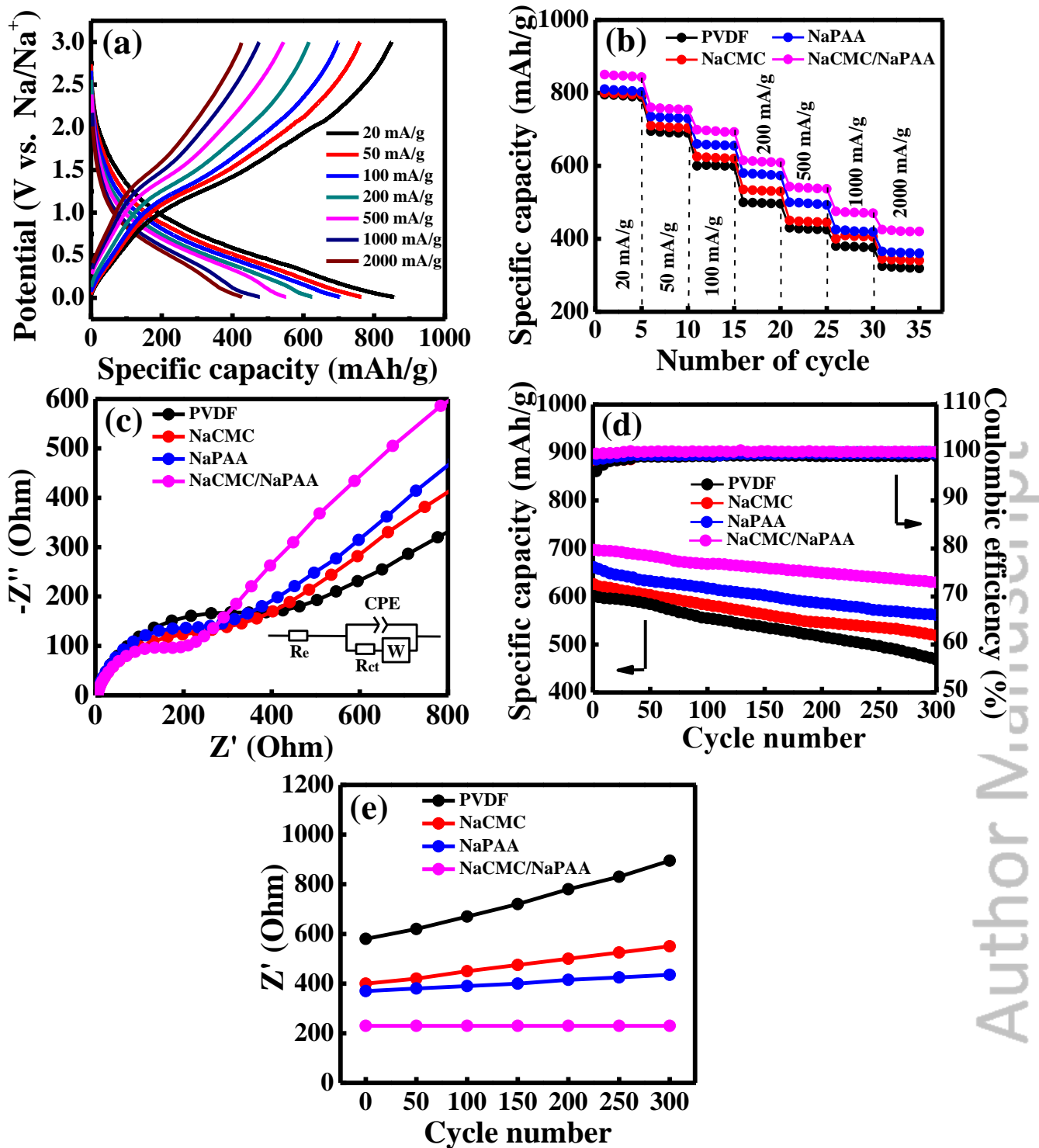**Figure 4.** Scheme of electrode structures with PVDF and NaCMC/NaPAA binders after charge–discharge cycling.

29

Figure 5. (a) Charge–discharge curves of NaCMC/NaPAA electrode measured at various rates. (b) Comparison of reversible capacities of various electrodes measured at various rates. (c) EIS data of the electrodes with various binders after conditioning cycles. (d) Cycling stability data of SnO_2@CMK-8 electrodes with various binders measured at 100 mA g^{-1}. (e) R_{ct} values of various electrodes with respect to charge–discharge cycle number.
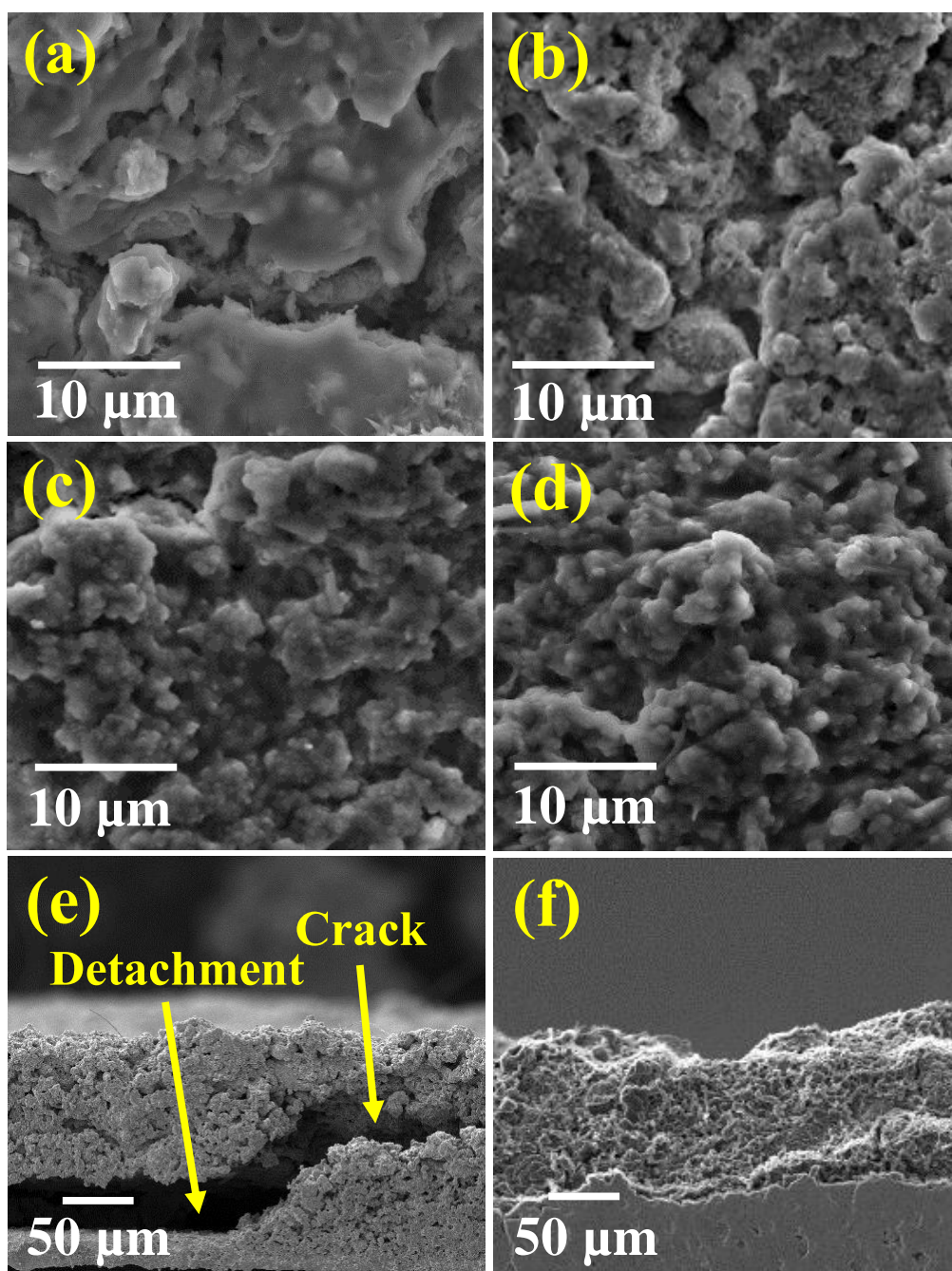
Figure 6. SEM images of SnO$_2$@CMK-8 electrodes with (a) PVDF, (b) NaCMC, (c) NaPAA, and (d) NaCMC/NaPAA binders after 300 charge–discharge cycles. FIB cross-section images of (e) PVDF and (f) NaCMC/NaPAA electrodes after the same cycles.
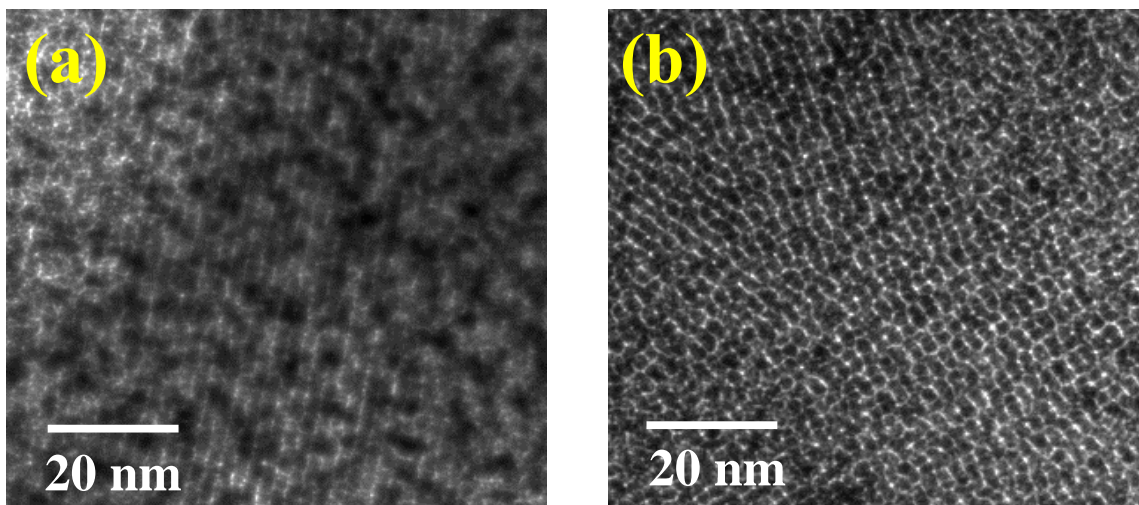
31

Figure 7. TEM images of SnO$_2$@CMK-8 samples with (a) PVDF and (b) NaCMC/NaPAA binders after 300 charge–discharge cycles.
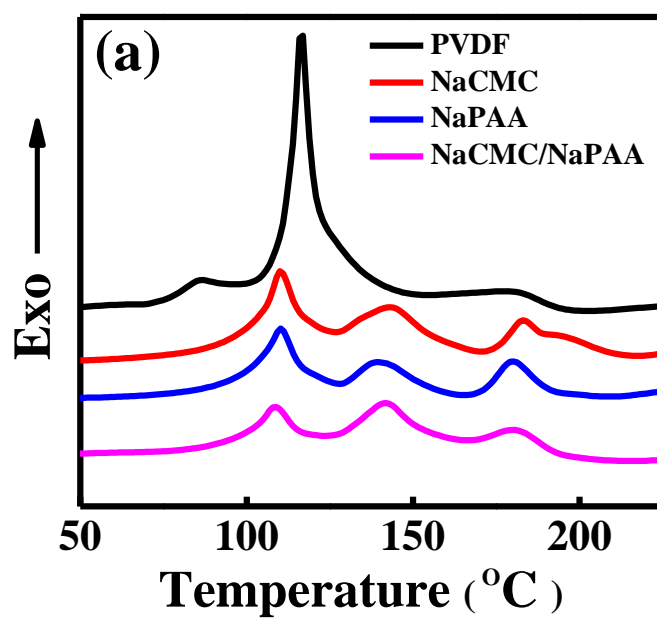
Figure 8. DSC data of sodiated SnO_2@CMK-8 samples with various binders.

The table of content entry

Binder selection is crucial to determine sodiation/desodiation kinetics, cycling stability, SEI growth, and even thermochemical stability of SnO$_2$@CMK-8 composite anodes.

Keywords: sodium battery, electrode mechanical integrity, binder wetting and spreading

Jagabandhu Patra, Purna Chandra Rath, Chi Li, Hsien-Ming Kao, Fu-Ming Wang, Ju Li[*], Jeng-Kuei Chang[*]

Water-soluble NaCMC/NaPAA binder for exceptional improvements of sodium-ion battery with SnO$_2$–ordered mesoporous carbon anode

34